

Motion of grains, droplets, and bubbles in fluid-filled nanopores

Nazar Sushko and Marek Cieplak

Institute of Physics, Polish Academy of Sciences, Aleja Lotnikow 32/46, 02-668 Warsaw, Poland

(Received 17 July 2000; published 16 July 2001)

Molecular dynamics studies of nanometer-sized rigid grains, droplets and bubbles in nanometer-sized pores indicate that the drag force may have a hydrodynamic form if the moving object is dense and small compared to the pore diameter. Otherwise, the behavior is nonhydrodynamic. The terminal speed is insensitive to whether the falling droplet is made of liquid or a solid. The velocity profiles within droplets and bubbles that move in the pore are usually nonparabolic and distinct from those corresponding to individual fluids. The density profiles indicate motional shape distortion of the moving objects.

DOI: 10.1103/PhysRevE.64.021601

PACS number(s): 68.03.Fg, 47.11.+j, 47.15.Gf, 66.20.+d

I. INTRODUCTION

Classical problems of motion of objects through fluids continue to be of interest because of their multiple applications in natural sciences and because of their frequent relation to fundamental issues. There is a variety of possible physical situations. The moving objects may be rigid or fluid. They may also span many length scales: from macroscopic, such as snowflakes [1] or sediments [2], to micrometer sized, such as water droplets and aerosols in clouds [3,4]. A new frontier arises in the context of micro- and nanoscale machinery [5,6] which sometimes involves flows through narrow pores. Two-phase flows in micro- and nanopores would require understanding of flows and interactions between nanometer-sized droplets. One recent example of this situation is provided by the surface force apparatus studies of capillary condensation in a nanoscale pore [7]. Droplets, bubbles, and grains of various sizes may move at various characteristic speeds. At large Reynolds numbers, smooth trajectories may become replaced by various classes of complex trajectories, like those observed in the motion of falling disks [8] or bubbles [9,10]. Another complexity may appear due to the droplet/bubble shape deformation, possibly combined with splitting and stacking [11,12], or due to a bubble collapse.

In this paper, we focus on issues arising at the molecular level aspects of such problems by considering nanometer-sized objects moving in larger but still nanometer-sized pores at low Reynolds numbers. Our interest is in probing the physics of nanoscale drag phenomena in simple molecular models and in assessing the validity of continuum physics concepts at this length scale. Our main purpose is to compare motion of droplets and bubbles to that of the solid spheres. The spheres are built of fluidlike atoms that are tethered to amorphyously located centers. Our studies are based on the molecular dynamics (MD) approach [13–17] which allows us to monitor motion of individual atoms, but its use is restricted to nanosecond time scales. Such atomic models should apply literally only to microscopic-scale systems but they may also be considered as toy models of larger droplets. Note also that rupture or coalescence of droplets [16,18–20], no matter how big, necessarily comes to a stage in which the interface morphology involves subcontinuum physics of nanoscale tendrils.

A natural way to study motion of an object in a fluid is to apply a driving force and determine the drag force F_d that brings the motion to a stationary state. Simulations on hard sphere systems [21,22,24] have indicated validity of Stokes' law [23]

$$F_d = 6\pi R\eta v, \quad (1)$$

down to atom-sized objects, when average quantities are monitored. In the Stokes' law above, R , η , and v denote, respectively, the radius of the moving sphere, the viscosity of the surrounding fluid, and the velocity of the body relative to an undisturbed fluid. However, the continuum mechanics predictions [25] break down and lead to divergent forces when one considers the approach of a sphere to a fixed wall at a constant velocity. The MD results [24], on the other hand, give evidence for a scenario in which the fluid atoms escape the region that is squeezed between the sphere and the wall, preventing any buildup in the force.

This paper provides a pilot MD study of the drag force phenomena that relate to the motion of droplets and bubbles. It is aimed at making a comparison to a similar MD analysis of solid nanoscale objects performed by Vergeles *et al.* [24]. We demonstrate that the drag force on droplets is similar to that on solid objects but the droplets undergo motional distortion. The MD results for the motion of droplets essentially agree with hydrodynamic predictions but this is not so in the case of the bubbles. The bubbles that we study have densities so low that they correspond to the crossover region between subcontinuum and continuum physics [26] and a nonhydrodynamic behavior, at such small length scales, is not surprising. Another interesting finding is that the surface tension effects at nanoscale confinement generally yield velocity profiles such that the velocity in the single fluid regions is quite distinct from that corresponding to one-fluid flows.

We start our analysis in Sec. II where construction of the nanoscale pore is described and properties of the fluid that fills it are established. The overall geometry is illustrated in Fig. 1 and the z direction corresponds to the pore axis. The primary role of the pore is to pin the fluid to its walls and thus to provide a stationary environment in which motion of falling objects can be studied. Our objective in this paper is focused on comparing various drag force phenomena at nanoscale length scale, as discussed within a simple molecu-

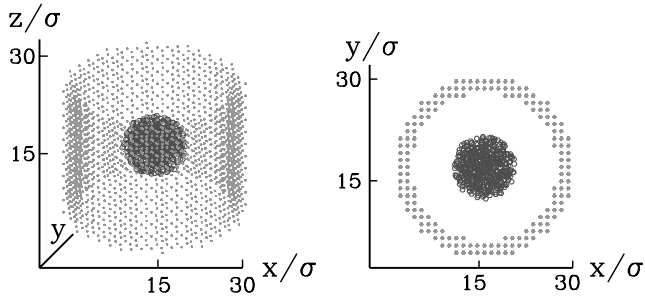


FIG. 1. A snapshot of solid sphere moving through a fluid-filled cylindrical pore. Only the solid and wall atoms are shown for clarity. The solid consists of 454 atoms that are tethered to amorphously placed centers. There are 2212 pore wall atoms which are fixed rigidly. The space between the solid and the pore is filled with 2281 fluid atoms (the case of fluid B). The left-hand figure represents a stereographic projection whereas the right-hand figure represents a projection from the top.

lar model of a generic nature, and not on the boundary phenomena arising near the confining wall. We take the wall to be built of Lennard-Jones atoms fixed rigidly on a fcc lattice and adjust parameters that minimize layering in the density profile near the wall. The reason is that it seems proper to consider first the simplest kind of drag phenomenon in which special wall-related effects are missing. Studies of near-the-wall physics and of excitations in the solid due to a flow would require considering a more realistic model, such as that used in studies of fluid flows in carbon nanotubes by Tuzun *et al.* [27].

We consider two kinds of fluid: one at a dense liquid density (*A*) and another at a dense gas density (*B*). Both are described by the Lennard-Jones potential

$$u_{LJ}(r) = 4\epsilon \left[\left(\frac{r}{\sigma} \right)^{-12} - d_{\alpha,\beta} \left(\frac{r}{\sigma} \right)^{-6} \right], \quad (2)$$

where ϵ and σ are the units of energy and distance, respectively (for krypton $\sigma = 0.357$ nm and $\epsilon/k_B = 201.9$ K). The parameter $d_{\alpha,\beta}$ is 1 for $\alpha = \beta = A$ and 0.5 for $\alpha = \beta = B$. This choice makes *B* more gaslike. We adopt the cutoff of 2.5σ in the potential. Our choice of parameters of the system, such as temperature, densities, and those related to the geometry and potentials of interactions, is ultimately geared toward generating a situation, by trial and error, in which the densities of fluids *A* and *B* are roughly the same in both the droplet and bubble cases. Thus the droplet made of fluid *A* that moves in fluid *B* is approximately a symmetric image—densitywise—of the bubble of fluid *B* that moves in fluid *A*.

In Sec. III, we discuss gravity driven motion down the *z* axis of a spherically shaped atomic solid. We present results on the density and velocity fields of the surrounding fluid and confirm the validity of Stokes' law. In Sec. IV, we discuss static properties of droplets of liquid *A* surrounded by fluid *B* and those of *B*-fluid bubbles immersed in liquid *A*. We consider the immiscible case in which $d_{A,B} = 0$. In Sec. V, we give illustrative examples of diffusional merger of the droplets in an environment unconstrained by any pore walls. In Secs. VI and VII, we return to the pore geometry and

consider motion of a single droplet and a single bubble under the influence of a gravitational force g . We consider two cases: either the g is applied only to the molecules of the droplet/bubble (Sec. VI), or it is applied to all of the molecules of the system (Sec. VII). In a true nanopore, the latter is more realistic. On the other hand, as a toy model, the former is easier to understand because this case mimics the situation in which the object moves in a stationary medium and in which only the immediate neighborhood of the object is disturbed. In other words, the case of the force acting only on the object corresponds conceptually to a motion in a much larger sized fluid than available in MD simulations.

II. THE SINGLE FLUID-FILLED NANOPORE

The geometry of the pore is shown in Fig. 1. The pore is constructed by first generating a fcc-like lattice in which subsequent sites in the *x*, *y*, and *z* directions differ by σ . The wall sites are obtained by cutting out an annulus of the inner and outer radii of 12σ and 15σ , respectively. The pore's axial length is 24σ and periodic boundary conditions are adopted along the *z* direction. The primary purpose of introducing the walls is to pin the fluid at the walls and allow for dissipation. Periodic boundary conditions in the *x* and *y* directions would not lead to establishment of the terminal speed. For simplicity, we keep the pore wall atoms frozen at their crystalline positions.

As is known from MD studies of channel flows [28–30] occurring between two parallel plates, the walls may induce a layered structure in the density profile on the scale of several σ in the neighborhood of the walls. The magnitude of this effect depends on the strength of the interaction between the fluid and the wall and on the fluid density. We adopt the Lennard-Jones interaction for the wall-fluid interaction with ϵ replaced by $\epsilon_{w,f} = 0.7\epsilon$. Our intention here is to provide some pinning (with a small slip length) and, at the same time, to minimize existence of the layered structure so that the density profile is as flat as possible. This particular value of $\epsilon_{w,f}$ was obtained by trial and error. Figure 2 shows the resulting density profiles for fluids *A* and *B*, obtained with 6554 and 2646 molecules, respectively. The densities at the central region are correspondingly $0.75\sigma^{-3}$ and $0.20\sigma^{-3}$. For fluid *B*, there is essentially one layer next to the wall and just a remnant of the second atomic layer beyond which the profile is flat. Larger values of $\epsilon_{w,f}$ would result in establishment of several layers. For liquid *A*, the intermolecular attraction is stronger than that due to the wall atoms, which results in a depletion layer near the wall, but the flat region in the center is large enough to accommodate a relatively large sized bubble of fluid *B*, as will be discussed later. The slip length for fluid *B* is smaller than for liquid *A* even though *B* is much more rarefied [30]. This is due to the different values of $d_{\alpha,\beta}$ in Eq. (2) but the same wall-fluid interactions for the two fluids.

A characteristic time scale $\tau = \sigma(m/\epsilon)^{1/2}$, where m is the mass of a fluid molecule (the masses of molecules in fluids *A* and *B* are identical), corresponds to the period of oscillations in the Lennard-Jones potential minimum of fluid *A*. The integration step was 0.005τ and the starting velocity distribu-

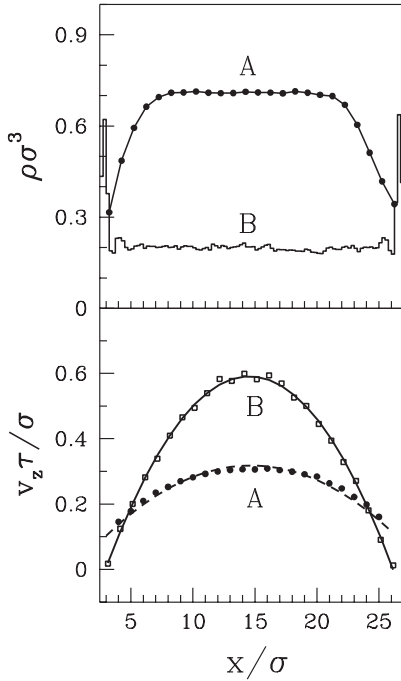


FIG. 2. The top panel shows the density profiles for fluids *A* and *B*, as indicated, obtained in a vertical cut through the pore. The cut is at $y=0$ and the data are averaged over the axial z direction. The bottom panel shows velocity profiles for fluids *A* and *B* under gravity driven flow with $g=0.01\epsilon/\sigma$. The corresponding central densities are $\rho=0.2/\sigma^3$ and $\rho=0.75/\sigma^3$.

tion was Maxwellian. Our thermostating procedure was based on Langevin noise [31] which balances the frictional dissipation. The equation of motion for the x coordinate of a molecule then reads

$$m\ddot{x} = F_c - \zeta\dot{x} + \Gamma, \quad (3)$$

where F_c is the force due to other molecules, $\zeta=0.005m/\tau$ is the coefficient of friction, and Γ is a Gaussian uncorrelated random force such that

$$\langle \Gamma(t)\Gamma(t') \rangle = 2\zeta T \delta(t-t'). \quad (4)$$

A similar equation holds for the other coordinates but no Langevin noise was applied in the z direction in order not to affect the systematic flows due to gravity, once it is switched on. The equations of motion are solved by means of a fifth order predictor-corrector scheme [14]. Throughout the paper, we report the calculations done at the temperature T of $0.71\epsilon/k_B$ at which there is sufficient stability of droplets of the size studied here. Another reason for this choice of T is that this is one of the several values chosen in the classic MD studies of droplets by Thompson *et al.* [32].

The viscosity of fluids *A* and *B* can be obtained from the velocity profiles, as shown in Fig. 2, by fitting to the parabolic form [33]

$$v = \frac{\rho g}{4\eta} (R_0^2 - r^2). \quad (5)$$

Here, R_0 is the effective radius of the cylinder, ρ denotes fluid density, and r is the polar coordinate. Our values of η for fluids *A* and *B* are $(2.22 \pm 0.12)m/\sigma\tau$ and $(0.23 \pm 0.04)m/\sigma\tau$, respectively.

III. MOTION OF SPHERICAL SOLID GRAINS

We begin our analysis by considering a gravity driven motion of a spherically shaped solid object in fluid *B*. Our model of the falling object is an amorphous variant of a model considered by Vergeles *et al.* [24]. We first take 454 points and place them randomly within a spherical volume with the density of $0.8/\sigma^3$. The corresponding radius is 5.1σ . These points are adopted as tethering centers for molecules of the same mass as that of the fluid molecules. The amorphousness is adopted for a more direct comparison to a liquid droplet which is amorphous but lacks the stiffness of the solid. The molecules of the solid are attracted to their tethering centers by a strong harmonic force with the spring constant of $400\epsilon/\sigma^2$.

The solid atoms in the bulk of the sphere just stay at the tethering centers but those near the surface experience, in addition to the elastic forces, interactions $u_{s,f}$ with the molecules of the fluid. We chose $u_{s,f}$ to be as between the fluid atoms, i.e., of the Lennard-Jones type:

$$u_{s,f}(r) = 4\epsilon \left[\left(\frac{r}{\sigma} \right)^{-12} - d_{s,f} \left(\frac{r}{\sigma} \right)^{-6} \right]. \quad (6)$$

We have considered three values of $d_{s,f}$: 0, 0.5, and 1. The first choice, of a pure repulsion, mimics the interactions between the *A* and *B* fluid molecules to allow comparisons with the droplet, and this is the choice we focus on most. The other choices allow the sphere to drag more fluid and perturb the environment more strongly.

We determine the motion of the solid atoms in two stages. First, we calculate what are the net force and torque with which the surrounding fluid acts on the whole solid. The tethering centers are then translated and rotated around the center of mass according to the values of these quantities. (We have found no systematic rotation in our studies.) In the second stage, we reevaluate the forces on the solid atoms (the elastic contributions come from tethers whose anchors have been moved) and then evolve the positions of the atoms according to the standard MD scheme. Gravitational forces, if any, are applied after an equilibration period of order 300τ .

Figure 3 shows the velocity of the center of mass as a function of time. The top panel is for $d_{s,f}=0$ and the bottom panel for two larger values of $d_{s,f}$. We observe the phenomenon of saturation—the center of mass velocity saturates at a terminal velocity v_t . The saturation level is a linear function of g and it decreases when $d_{s,f}$ is increased. The time scale to reach saturation is of order 200τ . From Eq. 1 for the grain we found the value of the terminal velocity to be equal to $v_t' = 0.203\tau/\sigma$ ($g=0.01\epsilon/\sigma$) and $v_t' = 1.019\tau/\sigma$ ($g=0.05\epsilon/\sigma$). These values are in good agreement with those obtained numerically when gravitational force is acting only on the atoms of the solid. For the case where this force is applied to all atoms Eq. (1) is not valid.

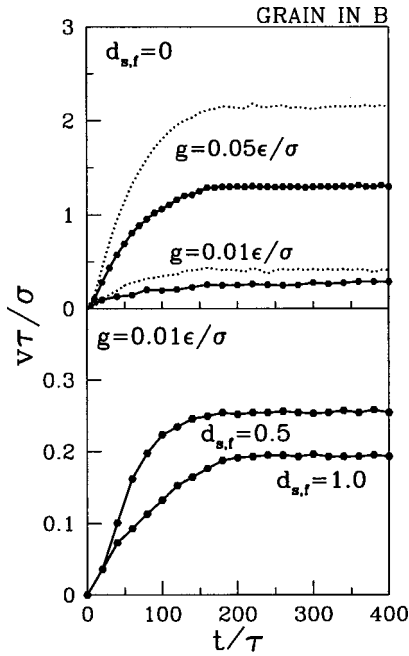


FIG. 3. Evolution of the velocity of the center of mass of the spherical solid in fluid B for the two different values of g as indicated in the figure. The solid lines correspond to the gravitational force acting only on the atoms of the solid whereas the dotted lines correspond to this force being applied to all atoms. The upper panel is for $d_{s,f}=0.5$ and the terminal velocities are, top to bottom, $2.148\sigma/\tau$, $1.297\sigma/\tau$, $0.441\sigma/\tau$, and $0.266\sigma/\tau$. The lower panel is for $g=0.01\epsilon/\sigma$ and it compares two values of $d_{s,f}$: 0.5 and 1. The terminal speeds are $0.254\sigma/\tau$ and $0.194\sigma/\tau$, respectively.

When the gravitational force is applied only to the atoms of the solid, the velocity field in the fluid is affected almost exclusively in the central region of the width that coincides with the sphere's diameter. If the force is applied to all atoms, the terminal speeds are larger since the fluid itself participates in the motion—this becomes a Poiseuille-like flow.

In Fig. 4 profiles of velocity of the spherical solid are

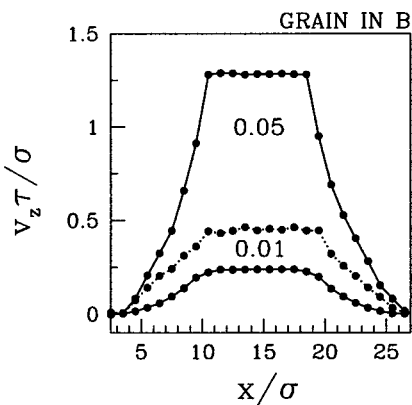


FIG. 4. The velocity profiles for the rigid spherical solid in a reference frame that moves with the grain and at the center of the grain. The solid lines correspond to the gravitational force acting only on the atoms of the solid whereas the dotted lines correspond to this force being applied to all atoms. The values of g , in units of ϵ/σ , are indicated.

shown. These profiles were obtained in a moving system of coordinates connected with the center of mass of the spherical solid. The atoms in the central region move rigidly.

IV. STATIC DROPLETS AND BUBBLES

There have been a number of MD studies of droplets. Among the more recent entries there are simulations of droplets that form during the rapid expansion of a liquid [34] and an analysis of the terraced spreading of a 2000-molecule droplet that lands on an atomic surface [35]. A comprehensive study of liquid droplets in equilibrium with their own vapor has been done by Thompson *et al.* [32]. They considered between 41 and 2004 Lennard-Jones molecules of a single kind. Still larger droplets have been simulated by Powles *et al.* [36,37]. The studies by Thompson *et al.* focus on quantities related to the phenomenon of surface tension. The authors provided a molecular level validation for (a) Laplace's equation for the pressure difference between the inside and outside of a droplet, (b) Kelvin's equation for the radius dependence of the vapor pressure, and (c) Tolman's equation for the effect of curvature on the coefficient of the surface tension. The profiles of the density obtained on radial crossing of the gas-liquid interface have been found to be well represented by the function

$$\rho(r) = \frac{1}{2}(\rho_l + \rho_v) - \frac{1}{2}(\rho_l - \rho_v)\tanh[2(r-R)/D_s], \quad (7)$$

where D_s is a measure of the thickness of the interface, R is an estimate of the droplet radius, ρ_l is the density of the liquid in the center of the droplet, and ρ_v denotes the density of the vapor far away from the interface. D_s depends on the gas-liquid interaction and it is usually of order several σ .

One theoretical device that was used by Thompson *et al.* [32] was to adopt the geometry of a spherical container that would scatter the molecules back to the system if they were about to leave it. When we studied droplets in a “vacuum” with periodic boundary conditions in all directions, we found that at each value of T and of ρ_l there is a threshold number of molecules below which the droplet evaporates and occupies all of the periodic volume. Above this threshold number the droplet remains stable and is surrounded by a few vapor molecules.

We have checked that at $T=0.71\epsilon/k_B$ a droplet of 454 atoms A , with an initial central density of about $0.8/\sigma^3$, is stable on its own without any spherical container. The stability properties are even more assured when such a droplet is immersed in the immiscible fluid B and this size of droplet has been adopted for further studies. The confining pore walls also add to the stability. Figure 5 shows the equilibrated density profile when the droplet is placed in the pore filled with 2281 molecules of fluid B . We observe that the droplet is well defined and is not immediately interacting with the pore walls. Its radius is about the same as of the spherical solid studied in the previous section—about 5.1σ . The profile at the interface is consistent with the tanh form given by Eq. (7).

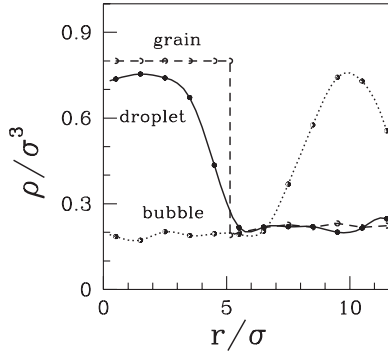


FIG. 5. The profile of the total density corresponding to (a) a droplet of liquid A immersed in fluid B (the solid line), (b) a bubble of fluid B immersed in liquid A (the dotted line), and (c) a spherical solid, of the same number of particles as the droplet, immersed in fluid B (the dashed line). The molecules occupy the pore space and the axial average has been performed—the profile is plotted vs the radius. The droplet data show an enhancement in the density next to the wall that corresponds to the first monolayer peak indicated in Fig. 2 without the axial averaging.

In order to generate a stable bubble, we surround 300 of the B -type molecules by 6145 A -type molecules. The equilibrated density profile is shown in Fig. 5. The corresponding radius is about 7.4σ . Thus the bubble is several σ 's away from the depletion zone. The density (and pressure) within the bubble is essentially uniform and it is around $0.2\sigma^{-3}$ —similar to that of the fluid in which the droplet and the grain move.

V. COALESCENCE OF DROPLETS

Before we continue with our analysis of the drag force phenomena in the pore geometry we pause for some discussion of coalescence of two initially independent droplets. Continuum mechanics provides no mechanism for coalescence and yet two droplets placed sufficiently close to each other may combine simply through atomic diffusion.

In order to show this, we first consider a volume of size $25 \times 25 \times 25$ with periodic boundary conditions. We form a single A -type droplet of 454 molecules in the center of the volume and surround it by 3751 molecules of type B (with the density of $0.2\sigma^{-3}$). After an equilibration period of 300τ , we double the volume of the system by placing its mirror replica in the z direction. This thus generates two droplets and the distance between their centers of mass is denoted by R_{12} . We have found that when R_{12} is bigger than 14.2σ the two droplets stay as separate and stable entities—at least during the time of 200τ and at $T = 0.71\epsilon/k_B$. Otherwise they merge diffusively as illustrated in Fig. 6. There appears to be no noticeable hydrodynamic velocity field related to the coalescence.

VI. GRAVITY DRIVEN FALL OF DROPLETS AND BUBBLES

We now return to the problem of the droplet or bubble motion in the pore and consider the case in which g is ap-

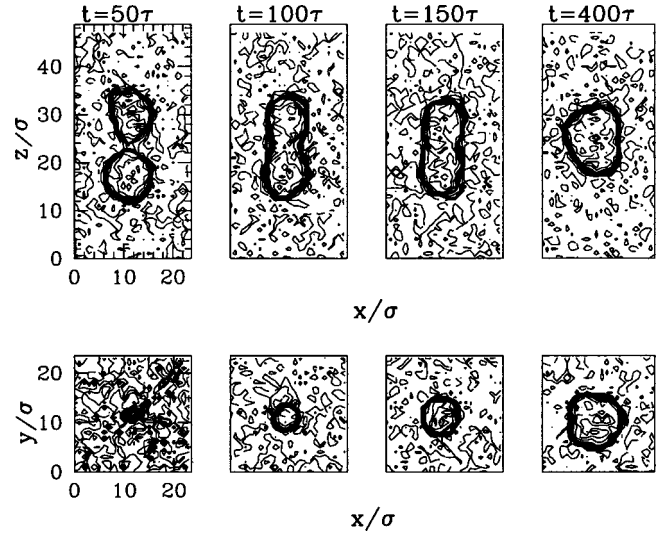


FIG. 6. The density contours of the droplets during coalescence. The data were time averaged over periods of 25τ . The top panels refer to a central cut in the xz plane. The bottom panels refer to a plane that is halfway between the initially separated droplets and later becomes an equatorial plane in the fused droplet.

plied only to the atoms of the moving object. We ask whether this motion is similar to that of the rigid amorphous solid.

A hydrodynamic prediction [38] for the drag force acting on a spherical liquid droplet or bubble of radius R is

$$F_d = 2\pi R \eta \frac{2\eta + 3\eta'}{\eta + \eta'} v, \quad (8)$$

where η is the viscosity of the surrounding fluid and η' is the viscosity of the fluid of which the moving object is made. This coincides with Stokes law [Eq. (1)] in the limit of $\eta' \rightarrow \infty$. In the other limiting case of the gas bubble, $\eta' \rightarrow 0$, we obtain

$$F_d = 4\pi R \eta v. \quad (9)$$

Determination of the terminal speed results from balancing the gravitational pull by the drag force combined with the buoyant force and then [38]

$$v_t = \frac{2R^2 g (\rho' - \rho) (\eta + \eta')}{3\eta (2\eta + 3\eta')}, \quad (10)$$

where ρ is the fluid density and ρ' is the moving body density. The sign of v_t agrees with g for droplets but is opposite to g for bubbles. In our MD simulations, the effects of buoyancy are not incorporated because of the imposition of periodic boundary conditions in the axial direction. The corresponding hydrodynamic formula for v_t corresponds to setting ρ in Eq. (10) to zero (and then both droplet and bubble move along the z direction). Due to diffuse density profiles, a more accurate comparison of MD to the hydrodynamic results is obtained by noting that in the stationary state F_d should be balanced by g times the number of molecules

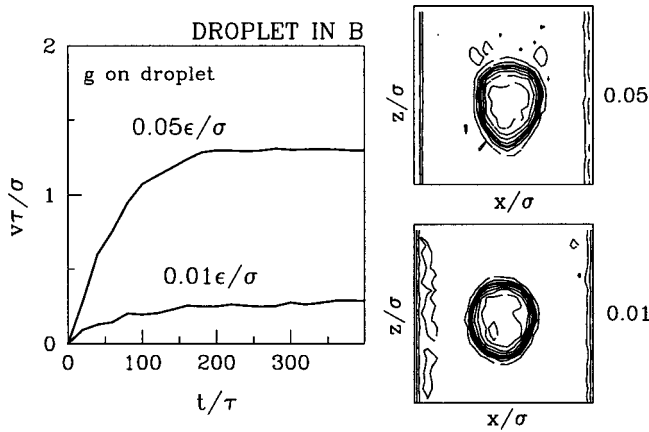


FIG. 7. Time evolution of the velocity of the mass center of the droplet for the two indicated values of g . The two panels on the right show the corresponding density contours in the stationary state. The thickest of the solid lines corresponds to one-half of the maximum value of the density.

in the moving object. The resulting v_t will be denoted as the hydrodynamic prediction and the values of viscosity are as determined by MD in Sec. II.

Results of our MD studies of the droplet motion are illustrated in Fig. 7. The left panel shows the time dependence of the velocity of the center of mass of the droplet. The effects of saturation arise after approximately 100τ and 150τ for $g = 0.01\epsilon/\sigma$ and $0.05\epsilon/\sigma$, respectively. The corresponding v_t are $(0.265 \pm 0.024)\sigma/\tau$ and $(1.293 \pm 0.021)\sigma/\tau$. The droplet is spherical initially and then it has a radius of 4.4σ . The right-hand panels of Fig. 7 for the density contours in the stationary state indicate that the droplet continues to be nearly spherical throughout the motion if g is sufficiently small. On the other hand, for $g = 0.05\epsilon/\sigma$, there is a noticeable stretching along the direction of motion (the axial and sideway radii differ by about 2.7σ).

The hydrodynamic prediction for v_t is $0.246\sigma/\tau$ for $g = 0.01$ if the initial value of R is 4.4σ . This agrees very well with the result of MD despite the perturbing effects of the

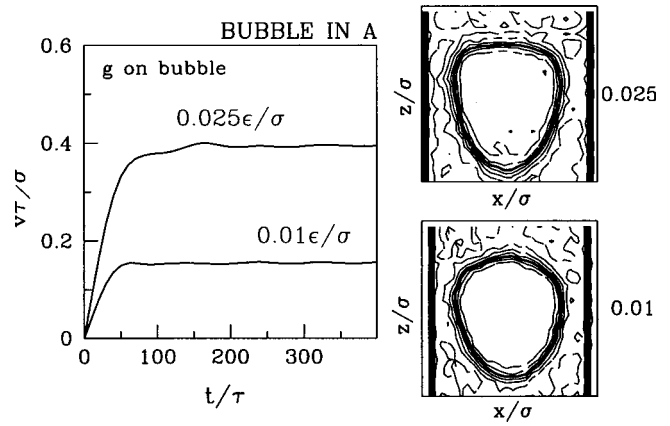


FIG. 9. Same as in Fig. 7 but for the bubble.

pore walls. This suggests that the continuum approach works also for motion of microscopic droplets. Note also that the values of v_t agree very well with those for a similarly built rigid grain—the center of mass moves virtually identically.

The velocity profiles, shown in Fig. 8, are quite similar to those shown in Fig. 4 except that there is a parabolic profiling in the region of the droplet.

Figure 9 shows that the saturation stage of a moving bubble is reached faster than in the case of the droplet and that the shape of the bubble is affected by the motion more heavily than the droplet. The bubble does not split and moves as a single entity, at least for g less than $0.025\epsilon/\sigma$. The bubble disintegrates for g of order $0.05\epsilon/\sigma$. The terminal velocities are $(0.154 \pm 0.07)\tau/\sigma$ and $(0.385 \pm 0.015)\tau/\sigma$ for $g = 0.01\epsilon/\sigma$ and $0.025\epsilon/\sigma$, respectively. The hydrodynamic prediction, however, yields v_t that is about 10 times smaller. This suggests that microscopic bubbles do not move hydrodynamically. The hydrodynamic behavior might be restored with a much wider pore but we had no capacity to test this hypothesis.

Despite the significant shape distortions, the velocity profiles (Fig. 8) for the bubble look very much like those for a falling frozen solid of a comparable density—there is no parabolicity in the center.

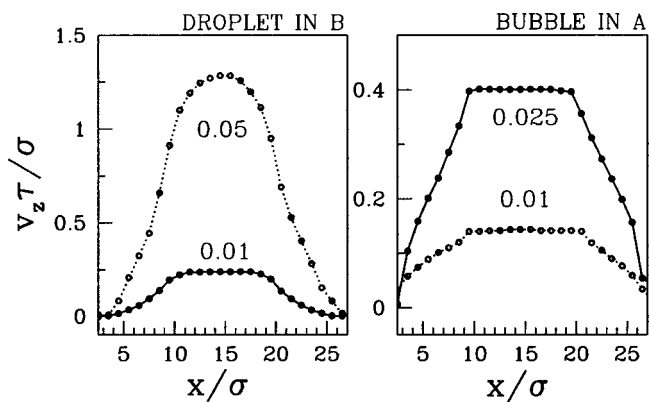


FIG. 8. The left panel shows velocity profiles for a droplet accelerated by force g with the values (in units of ϵ/σ) as indicated. The right-hand panel shows velocity profiles for the bubble.

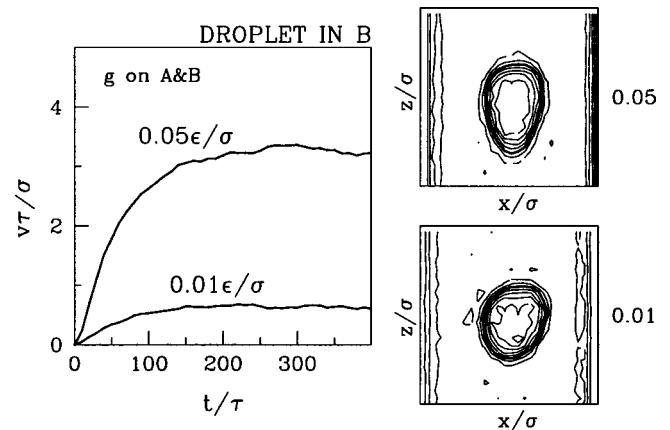


FIG. 10. Same as in Fig. 7 but for g applied to all atoms within the pore space.

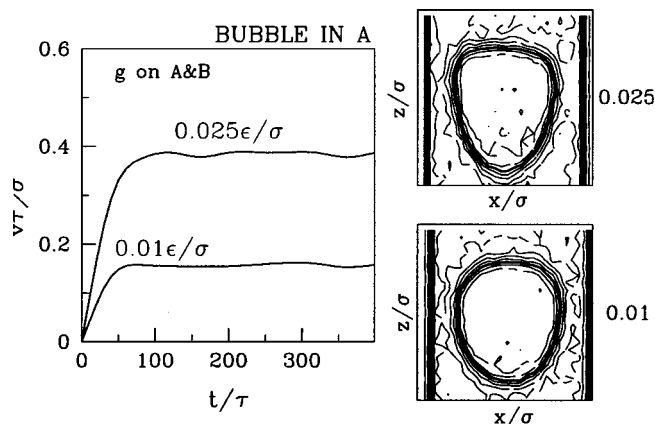


FIG. 11. Same as in Fig. 9 but for g applied to all atoms within the pore space.

VII. GRAVITY DRIVEN FLOW WITH DROPLETS OR BUBBLES

We now consider the situation in which the gravitational force is applied to all molecules in the pore space. This is then two-phase gravity driven flow.

We find that the terminal velocities are now about 2.7 times bigger than the hydrodynamic prediction would yield even though the fluid right next to the pore wall is almost pinned. For the droplet, v_t is $(0.672 \pm 0.018)\sigma/\tau$ and $(3.272 \pm 0.023)\sigma/\tau$ for $g=0.01$ and $0.05\epsilon/\sigma$, respectively. For the bubble, v_t is almost the same as when g was applied only to the molecules of the bubble. For instance, v_t is $(0.157 \pm 0.011)\sigma/\tau$ for $g=0.01\epsilon/\sigma$. These results together indicate that when velocity profiling outside the moving object becomes significant the drag force deviates from the simple form given in Eq. (8).

The density profiles shown in Figs. 10 and 11 are close to those shown in Figs. 7 and 9, respectively, but the axial stretching is a bit stronger.

Figure 12 shows the velocity profiles, in the moving frame of reference, when g is applied to all molecules within the pore, and compares them to the single fluid results as replotted from Fig. 2. Both the droplet and the bubble continue to have velocity profiles that are flat in the center. When compared to the situation in which g is applied only to

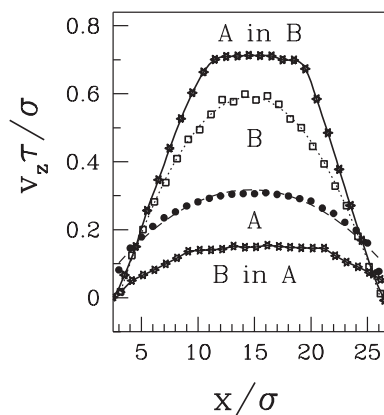


FIG. 12. The velocity profiles when g of $0.01\epsilon/\sigma$ is applied to all atoms within the pore. The top and bottom curves refer to the droplet and bubble cases, respectively. The data points marked by A and B are the same as in the lower panel of Fig. 2.

the moving object, as in Fig. 8, the velocity profile of the droplet is significantly enhanced. This is consistent with the enhanced values of the terminal velocity. On the other hand, the velocities around the center of the bubble are slightly reduced. It is interesting to note that, in the central region, the droplet moves faster than any of the constituting fluids at the same value of g . For the bubble, it is the other way around. The existence of this effect may depend on the geometry and viscosities involved. In each case, however, the velocity profile determined in slices that are vertically away from the droplet or the bubble agree with the single fluid results of Fig. 2.

We conclude by noting that the drag force appears to have the simple hydrodynamic form if the moving object is dense and small compared to the pore diameter. Otherwise, the velocity field is significantly disturbed by the pore and the drag force becomes more complicated. It may also be sensitive to the nature of interactions between the pore wall and fluid atoms.

ACKNOWLEDGMENT

This research was supported by a grant from the Polish agency KBN (Grant No. 2P03B-025-13).

-
- [1] M. Kajikawa, *J. Meteorol. Soc. Jpn.* **60**, 797 (1982).
 [2] J. R. L. Allen, *Sedimentology* **31**, 227 (1984).
 [3] H. R. Pruppacher and J.D. Klett, *Microphysics of Clouds and Precipitation* (Reidel, Dordrecht, 1978).
 [4] J. H. Seinfeld and S. N. Pandis, *Atmospheric Chemistry and Physics* (Wiley, New York, 1998).
 [5] *Microelectromechanical Systems (MEMS)*, edited by C.-J. Kim (American Society of Mechanical Engineers, New York, 1997).
 [6] C.-M. Ho and Y.-C. Tai, *Annu. Rev. Fluid Mech.* **30**, 579 (1998).
 [7] M. M. Kohonen, N. Maeda, and H. K. Christenson, *Phys. Rev. Lett.* **82**, 4667 (1999).
 [8] S. B. Field, M. Klaus, M. G. Moore, and F. Nori, *Nature (London)* **388**, 252 (1997).
 [9] E. Kelley and M. Wu, *Phys. Rev. Lett.* **79**, 1265 (1997).
 [10] R. Krishna and J. M. van Baten, *Nature (London)* **398**, 208 (1999).
 [11] T. Maxworthy, *J. Fluid Mech.* **173**, 95 (1986).
 [12] D. W. Moore, *J. Fluid Mech.* **23**, 749 (1965).
 [13] J. M. Haile, *Molecular Dynamics Simulations: Elementary Methods* (Wiley, New York, 1993).
 [14] M. D. Allen and D. J. Tildesley, *Computer Simulation of Liquids* (Oxford University Press, New York, 1993).
 [15] G. Ciccotti and W. G. Hoover, *Molecular Dynamics Simula-*

- tion of Statistical Mechanics Systems* (North Holland, Amsterdam, 1986).
- [16] J. Koplik and J. R. Banavar, *Annu. Rev. Fluid Mech.* **27**, 257 (1995).
- [17] J. Koplik and J. R. Banavar, *Comput. Phys.* **12**, 424 (1998).
- [18] J. Koplik and J. R. Banavar, *Science* **257**, 1664 (1992).
- [19] J. Koplik and J. R. Banavar, *Phys. Fluids A* **5**, 521 (1993).
- [20] M. Cieplak, *Phys. Rev. E* **51**, 4353 (1995).
- [21] B. J. Alder and T. E. Wainwright, *Phys. Rev. A* **1**, 18 (1970).
- [22] W. E. Alley and B. J. Alder, *Phys. Rev. A* **27**, 3158 (1983).
- [23] G. G. Stokes, *Proc. Cambridge Philos. Soc.* **9**, 8 (1851).
- [24] M. Vergeles, P. Keblinski, J. Koplik, and J. R. Banavar, *Phys. Rev. Lett.* **75**, 232 (1995).
- [25] H. Brenner, *Chem. Eng. Sci.* **16**, 242 (1961).
- [26] M. Cieplak, J. Koplik, and J. R. Banavar, *Phys. Rev. Lett.* **86**, 803 (2001).
- [27] R. E. Tuzun, D. W. Noid, B. G. Sumpter, and R. C. Merkle, *Nanotechnology* **7**, 241 (1996).
- [28] J. Koplik, J. R. Banavar, and J. F. Willemsen, *Phys. Fluids A* **1**, 781 (1989).
- [29] P. A. Thompson and M. O. Robbins, *Phys. Rev. A* **41**, 6830 (1990).
- [30] M. Cieplak, J. Koplik, and J. R. Banavar, *Physica A* **274**, 281 (1999); **287**, 153 (2000).
- [31] W. F. van Gunsteren and H. J. C. Berendsen, *Mol. Phys.* **45**, 637 (1982).
- [32] S. M. Thompson, K. E. Gubbins, J. P. R. B. Walton, R. A. R. Chantry, and J. S. Rowlinson, *J. Chem. Phys.* **81**, 530 (1984).
- [33] G. K. Batchelor, *An Introduction to Fluid Dynamics* (Cambridge University Press, Cambridge, England, 1967).
- [34] Wm. T. Ashurst and B. L. Holian, *Phys. Rev. E* **59**, 6742 (1999).
- [35] J.-X. Yang, J. Koplik, and J. R. Banavar, *Phys. Rev. A* **46**, 7738 (1992).
- [36] J. G. Powles, R. F. Fowler, and W. A. B. Evans, *Chem. Phys. Lett.* **96**, 289 (1983).
- [37] J. G. Powles, R. F. Fowler, and W. A. B. Evans, *Phys. Lett.* **98A**, 421 (1983).
- [38] W. Rybczynski, *Acad. Sci. Cracovie* **1A**, 40 (1911), as quoted by L. D. Landau and E. M. Lifshitz, *Hydrodynamics* (Nauka, Moscow, 1988), Chap. 20.